

# **IDEA League**

MASTER OF SCIENCE IN APPLIED GEOPHYSICS  
RESEARCH THESIS

---

## **Seismic deblending of simultaneous crossline sources**

**Christian Reinicke Urruticoechea**

---

July 14, 2015



# **Seismic deblending of simultaneous crossline sources**

MASTER OF SCIENCE THESIS

for the degree of Master of Science in Applied Geophysics at  
Delft University of Technology  
ETH Zürich  
RWTH Aachen University  
by

Christian Reinicke Urruticoechea

July 14, 2015

Department of Geoscience & Engineering	.	Delft University of Technology
Department of Earth Sciences	.	ETH Zürich
Faculty of Georesources and Material Engineering	.	RWTH Aachen University



**Delft University of Technology**

Copyright © 2013 by IDEA League Joint Master's in Applied Geophysics:

Delft University of Technology, ETH Zürich, RWTH Aachen University

All rights reserved.

No part of the material protected by this copyright notice may be reproduced or utilized in any form or by any means, electronic or mechanical, including photocopying or by any information storage and retrieval system, without permission from this publisher.

Printed in The Netherlands, Switzerland, Germany

IDEA LEAGUE  
JOINT MASTER'S IN APPLIED GEOPHYSICS

Delft University of Technology, The Netherlands  
ETH Zürich, Switzerland  
RWTH Aachen, Germany

Dated: *July 14, 2015*

Supervisor(s):

---

Dr. Ir. G.J.A. van Groenestijn

---

Dr. Ir. G.G.Drijkoningen

Committee Members:

---

Dr. Ir. G.J.A. van Groenestijn

---

Dr. Ir. G.G.Drijkoningen

---

Dr. Christoph Clauser



---

## **Abstract**

This is the shortest abstract you have ever seen.



---

## Acknowledgements

First of all I want to thank all the people who have participated in this project .. Remember, often more people have contributed to your final thesis than you initially would think of.

Delft, University of Technology  
July 14, 2015

Christian Reinicke Urruticoechea



---

# Table of Contents

<b>Abstract</b>	v
<b>Acknowledgements</b>	vii
<b>Nomenclature</b>	xvii
<b>Acronyms</b>	xvii
<b>1 Introduction</b>	1
<b>I Theory</b>	3
<b>2 Theory</b>	5
2-1 The Forward Model of Blending . . . . .	5
2-1-1 Conventional Seismic Data . . . . .	5
2-1-2 Blended Seismic Data . . . . .	7
2-2 Deblending . . . . .	9
2-2-1 Pseudo-Deblending . . . . .	9
2-2-2 Common Receiver Gather . . . . .	10
2-2-3 Iterative Estimation of Blending Noise . . . . .	10
<b>3 Incoherency</b>	15
3-1 Analysis of the Blending Matrix . . . . .	15
3-2 Effect of Incoherency . . . . .	18
3-3 Results . . . . .	20
3-4 Effect of Maximum Firing Time Delay . . . . .	20
3-5 Results . . . . .	20

<b>4 Crossline Deblending (3D)</b>	<b>21</b>
4-1 Data Sorting . . . . .	21
4-2 3D f-k-k Filter . . . . .	24
4-3 Results . . . . .	26
<b>5 Results on Synthetic Data</b>	<b>29</b>
5-1 Blending pattern . . . . .	29
5-2 Feasibility . . . . .	34
<b>6 Incoherency</b>	<b>35</b>
6-1 Incoherency Control Factors . . . . .	35
6-2 Quantification of Incoherency . . . . .	36
6-3 Optimization of Incoherency . . . . .	37
6-4 Fingerprint of the Incoherency in the Blending Matrix $\Gamma$ . . . . .	37
<b>Bibliography</b>	<b>39</b>
<b>A The back of the thesis</b>	<b>41</b>
A-1 An appendix section . . . . .	41
A-1-1 An appendix subsection with C++ Lisitng . . . . .	41
A-1-2 A MATLAB Listing . . . . .	41
<b>B Yet another appendix</b>	<b>43</b>
B-1 Another test section . . . . .	43

---

# List of Figures

2-1	Illustration of the data matrix, $\mathbf{P}$ , by van Groenestijn (2010). <i>Left:</i> The signal generated at the source position, $x_s$ , is measured at receiver position, $x_r$ , as a function of time, $t$ . Thus, the discretized data is saved in a cube, $\mathbf{p}(t, \mathbf{x}_r, \mathbf{x}_s)$ . <i>Right:</i> The cube on the right equals the left cube after a Fourier transform with respect to time. Each frequency slice of the right cube represents the data matrix, $\mathbf{P}$ . . . . .	6
2-2	Illustration of the data matrix, $\mathbf{P}$ , by Mahdad et al. (2011). The dotted lines indicate directions of common gathers. . . . .	6
2-3	(a) A conventional source matrix, $\mathbf{S}$ , is transformed to a blended source matrix, $\mathbf{S}_{bl}$ , by applying the blending matrix, $\Gamma$ . Each star represents a source, and the gray scale of the stars represents the relative firing time. (b) Illustration of conventional acquisition with one vessel. This acquisition set up is modeled by the source matrix $\mathbf{S}$ . (c) Illustration of blended acquisition with two vessels. In this case the blended source matrix $\mathbf{S}_{bl}$ models the acquisition set up. The experiment number is indicated on top of each drawing. . . . .	7
2-4	Common shot gather of two blended shots. The shot on the right is fired 120 ms after the left shot. . . . .	8
2-5	Flowchart belonging to the deblending method of Mahdad et al. (2011). . . . .	9
2-6	Pseudo-deblended data, $\mathbf{P}_{ps}$ , sorted in common shot gathers (a,b) and in a common receiver gather (c). The pseudo-deblended data of the right shot (a) and the left shot (b,c) were shifted by different time delays. The overlapping sources map in the pseudo-deblended shot gathers as coherent events, while they map as incoherent spikes in the pseudo-deblended receiver gather. . . . .	10
2-7	(a) Pseudo-deblended receiver gather. The subfigures (b)-(f) illustrate each step of the deblending algorithm. For better visibility examples from the 5 <sup>th</sup> iteration are chosen. (b) $f$ - $k$ -spectrum before (top) and after (bottom) $f$ - $k$ -filtering, (c) $f$ - $k$ -filtered common receiver gather, (d) after thresholding, (e) estimated blending noise, (f) estimated data. . . . .	11
2-8	. . . . .	12
2-9	Common receiver gather of the estimated data after 1, 5, 10, 15, 20 and 25 iterations. . . . .	14

3-1	Illustration of the matrix product, $\Gamma\Gamma^H$ . In this notation $\Delta t_k$ refers to the phase shift of the shot $k$ , and $\Delta t_{kl}$ refers to the phase shift between the shots $k$ and $l$ , $\Delta t_{kl} = \Delta t_k - \Delta t_l$ . . . . .	16
3-2	Comparison of the pseudo-deblended receiver gather for (a) constant firing time delays of 100 ms, and (b) random firing time delays between 0 ms and 100 ms. (c) and (d) show the $f$ - $k$ -spectra of (a) and (b) respectively. . . . .	17
3-3	The blending matrix, $\Gamma$ , is obtained by interchanging the 3 <sup>rd</sup> and 4 <sup>th</sup> row of the blending matrix in Figure 3-1. In acquisition this is equivalent to moving shot 3 to experiment 2, and shot 4 to experiment 1. A random permutation of the rows of the blending matrix spreads the off-diagonal elements of the matrix product, $\Gamma\Gamma^H$ . The elements are not assembled on the sub-diagonals anymore. . . . .	17
3-4	Illustration of the sub-diagonal elements in the complex number plane. The elements have unit length and variable phase. The absolute value of their sum depends on the phase coherency of the elements. . . . .	19
3-5	Illustration of the absolute sub-diagonal sums, $S(d, \omega)$ , for the frequency slice $f = 25$ Hz. (a) refers to the blending matrix $\Gamma_{coh}$ with coherent firing time delays. $S(d, \omega)$ is less spike-like and yields an incoherency value of $\mu_a = 67\%$ . (b) refers to the blending matrix $\Gamma_{ran}$ with random firing time delays. $S(d, \omega)$ is close to a spike and yields an incoherency value of $\mu_b = 98\%$ . . . . .	20
4-1	Illustration of the data matrix $\mathbf{P}$ for 3D data (van Dedem, 2002). $y_r$ and $y_s$ represent the inline receiver and source positions. $x_r$ and $x_s$ represent the crossline receiver and source positions. Each row refers to a 3D common receiver gather and each column to a 3D common shot gather. A sub-matrix with fixed receiver and source inline positions ( $y_r, y_s$ ) is equivalent to a data matrix for 2D acquisition. . . . .	22
4-2	(a) Common receiver gather of a 3D data set with crossline (x) and inline (y) sources. (b) Resorted data set. Individual crossline sections are plotted next to each other in 2D. For visibility both subfigures only show a reduced part of the data. . . . .	23
4-3	Illustration of the blending matrix, $\Gamma$ , for 3D acquisition. (a) At each of the $Ns_y$ inline position the crossline sources (x direction) are blended. Each of these 2D blending processes is described by a 2D blending matrix, which has as many rows as there are crossline sources, $Ns_x$ . (b) The 2D blending matrices are assembled in a single 3D blending matrix, $\Gamma$ , which has $Ns_x$ by $Ns_y$ rows. . . . .	23
4-4	One can design a 2D $f$ - $k_x$ -filter for 3D data. (a) shows a 40 Hz frequency slice of the $f$ - $k_x$ - $k_y$ spectrum, where the white area equals 1 and the black area is 0. Note that the filter is not affecting the inline wavenumbers $k_y$ . (b) illustrates the 2D $f$ - $k_x$ -filter sorted according to section 4-1. Each cone represents a 2D $f$ - $k$ -filter for a single inline wavenumber. . . . .	24
4-5	Illustration of the 3D $f$ - $k_x$ - $k_y$ -filter. (a) is a 40 Hz frequency slice of the $f$ - $k_x$ - $k_y$ spectrum of the data in Figure 4-2b. $k_x$ and $k_y$ refer to the crossline and inline wavenumber respectively. (b) shows the same data slice sorted in a 3D cube. The red cone represents the 3D $f$ - $k_x$ - $k_y$ filter mask. (c) is a 40 Hz frequency slice of the mask, where the white area equals 1 and the black area is 0. (d) and (e) display the $f$ - $k_x$ - $k_y$ data spectrum and mask sorted according to section 4-1, i.e. each sub-cone refers to one inline wavenumber. Note that due to the sorting the wavenumber axis is a mix of crossline and inline wavenumbers. For this reason the wavenumber axis has no labels. . . . .	25
4-6	The crossline sources of the synthetic data in Figure 5-1a are blended. Then, the 3D deblending algorithm is applied. In case (a) the algorithm uses a 2D $f$ - $k_x$ filter. In case (b) it uses a 3D $f$ - $k_x$ - $k_y$ filter. . . . .	27

4-7	Comparison of the deblending quality with a 2D $f-k_x$ filter and a 3D $f-k_x-k_y$ filter. The data in Figure 4-6a are blended with varying maximum firing time delay. Then the blended data are deblended using a 2D $f-k_x$ filter and a 3D $f-k_x-k_y$ filter. . . . .	27
5-1	These 3D common receiver gathers are sorted according to section 4-1. The unblended synthetic data (a) is used to simulate a blended acquisition with 3 experiments per crossline and 7 shots per experiment. The maximum firing time delay is 400 ms. The sources are blended in three different patterns: (b) Randomly selected sources are blended without time delay, (c) neighboring sources are blended with random time delays, (d) randomly picked sources are blended with random time delays. Next, the blended data sets are deblended. The corresponding deblending results are illustrated in (b) to (d). . . . .	31
5-2	(a)-(d) show inline slices of the data shown in Figure 5-1. (e)-(h) display the corresponding crossline slices. . . . .	32
5-3	Quality factor, $Q$ , as a function of the incoherency, $\mu$ . The quality factor is a measure for the deblending performance. The deblending results for quality factors above 5 look acceptable. . . . .	33
5-4	The 3 suggested blending patterns are simulated with maximum firing time delays between 40 ms and 400 ms. The quality factors are computed with respect to the unblended data and illustrated as a function of the maximum firing time. . . . .	34
5-5	Illustration of the acquisition design of the synthetic data in Figure 5-1. There are 21 sources in the crossline with a spacing of 12.5 m. At each inline position the crossline sources are blended in 3 experiments with 7 sources per experiment. . . . .	34



---

## **List of Tables**



---

## **Acronyms**

**DUT** Delft University of Technology



---

# Chapter 1

---

## Introduction

Welcome to the standard layout for your IDEA LEAGUE MSc thesis written in L<sup>A</sup>T<sub>E</sub>X. L<sup>A</sup>T<sub>E</sub>X has a variety of advantages over conventional/ standard text editing programs, which you will soon enough discover yourself. L<sup>A</sup>T<sub>E</sub>X almost forms a standard in the Scientific Community, especially due to its effective and straightforward mathematical capabilities.

This is Chapter 1. If you want to know more about L<sup>A</sup>T<sub>E</sub>X you better read ? or use the extensive help available on the internet. . This 'hidden' index command helps you making an index at the end of your thesis. You can add this flag anywhere you want to make an index hit. You can see here also how to use acronyms, like Delft University of Technology ([DUT](#)). The acronyms are automatically listed in the corresponding section. Also, hyperlinks are created automatically with the developed class file, such that your digital PDF version of your thesis can be read dynamically. Have fun with L<sup>A</sup>T<sub>E</sub>X and your M.Sc. research project and good luck!

The purpose of the introduction is to tell readers why they should want to read what follows the introduction. This chapter should provide sufficient background information to allow readers to understand the context and significance of the problem. This does not mean, however, that authors should use the introduction to rederive established results or to indulge in other needless repetition. The introduction should (1) present the nature and scope of the problem; (2) review the pertinent literature, within reason; (3) state the objectives; (4) describe the method of investigation; and (5) describe the principal results of the investigation.



# **Part I**

# **Theory**



---

# Chapter 2

---

## Theory

This chapter describes the theory behind blending and deblending. First the detail hiding operator notation is explained. This notation is used to describe the forward model of seismic data. By introducing the blending operator the forward model is extended to the blended case. Next, the deblending method presented in [Mahdad et al. \(2011\)](#) is discussed to illustrate some of the concepts used in this thesis.

### 2-1 The Forward Model of Blending

#### 2-1-1 Conventional Seismic Data

In the detail hiding operator notation ([Berkhout, 1982](#)) the recorded signal is considered discrete in terms of time  $t$ , receiver position  $x_r$ , and source position  $x_s$ . Thus, the measurements can be organized in a cube,  $\mathbf{p}(t, \mathbf{x}_r, \mathbf{x}_s)$  (see Figure 2-1). Each frequency slice of this new cube represents the data matrix,  $\mathbf{P}$ .

In the data matrix,  $\mathbf{P}$ , each column corresponds to a monochromatic common shot gather (see Figure 2-2), each row to a monochromatic common receiver gather, each diagonal to a monochromatic common offset gather, and each anti-diagonal to a monochromatic common midpoint gather.

According to the seismic forward model of [Berkhout \(1982\)](#) the data matrix,  $\mathbf{P}$ , can be represented by a matrix multiplication of the source matrix,  $\mathbf{S}$ , the impulse response of the earth,  $\mathbf{X}$ , and the receiver matrix,  $\mathbf{D}$ :

$$\mathbf{P} = \mathbf{D} \mathbf{X} \mathbf{S}. \quad (2-1)$$

In the source matrix,  $\mathbf{S}$ , each row and each column represent one source position (see Figure 2-3a). Thus,  $\mathbf{S}$  is a diagonal matrix. Each diagonal element  $s_{ii}$  captures one frequency component of the source signature injected in the earth at the position  $x_s = x_i$ . By applying



**Figure 2-1:** Illustration of the data matrix,  $\mathbf{P}$ , by [van Groenestijn \(2010\)](#). *Left:* The signal generated at the source position,  $x_s$ , is measured at receiver position,  $x_r$ , as a function of time,  $t$ . Thus, the discretized data is saved in a cube,  $p(t, x_r, x_s)$ . *Right:* The cube on the right equals the left cube after a Fourier transform with respect to time. Each frequency slice of the right cube represents the data matrix,  $\mathbf{P}$ .



**Figure 2-2:** Illustration of the data matrix,  $\mathbf{P}$ , by [Mahdad et al. \(2011\)](#). The dotted lines indicate directions of common gathers.



**Figure 2-3:** (a) A conventional source matrix,  $\mathbf{S}$ , is transformed to a blended source matrix,  $\mathbf{S}_{bl}$ , by applying the blending matrix,  $\boldsymbol{\Gamma}$ . Each star represents a source, and the gray scale of the stars represents the relative firing time. (b) Illustration of conventional acquisition with one vessel. This acquisition set up is modeled by the source matrix  $\mathbf{S}$ . (c) Illustration of blended acquisition with two vessels. In this case the blended source matrix  $\mathbf{S}_{bl}$  models the acquisition set up. The experiment number is indicated on top of each drawing.

a Fourier transform to all frequency components of the element  $s_{ii}$  the source signature is obtained.

The impulse response of the earth,  $\mathbf{X}$ , describes how an impulse at the source location,  $x_s$ , is transformed in the earth into the signal at the receiver location,  $x_r$ .

$\mathbf{D}$  is the receiver matrix, which converts the seismic wavefield at the receiver location  $x_r$  to the recorded signal. This includes the forward model of the receiver ghost.

In practice, one tries to retrieve the unknown earth response,  $\mathbf{X}$ , from the data,  $\mathbf{P}$ , by removing  $\mathbf{S}$  (designation) and  $\mathbf{D}$  (receiver deghosting).

### 2-1-2 Blended Seismic Data

For blended acquisition the recorded events belonging to different sources overlap as shown in the shot gather in Figure 2-4.

Blending can be captured in the forward model by introducing a blending matrix,  $\boldsymbol{\Gamma}$ , which transforms the source matrix,  $\mathbf{S}$ , into a blended source matrix,  $\mathbf{S}_{bl}$ ,



**Figure 2-4:** Common shot gather of two blended shots. The shot on the right is fired 120 ms after the left shot.

$$\mathbf{S}_{bl} = \mathbf{S} \boldsymbol{\Gamma}. \quad (2-2)$$

Each row of  $\boldsymbol{\Gamma}$  represents one source, and each column of  $\boldsymbol{\Gamma}$  represents one experiment (see Figure 2-3).

The blending matrix captures the physics of a blended acquisition as follows: An element  $\gamma_{ij}$  of the blending matrix includes a source  $i$  and an experiment  $j$ . If the source  $i$  is not fired in the  $j^{th}$  experiment the amplitude  $A_{ij}$  is zero. If it is fired, source  $i$  has a relative amplitude  $A_{ij}$  and a relative time delay  $t_{ij}$  with respect to the first source fired in the  $j^{th}$  experiment;

$$\gamma_{ij} = A_{ij} e^{-j\omega \Delta t_{ij}}. \quad (2-3)$$

Thus, the blending matrix selects specific sources from the source matrix and superimposes as visualized in Figure 2-3. From Figure 2-3 it also becomes clear that both the blending matrix,  $\boldsymbol{\Gamma}$ , and the blended source matrix,  $\mathbf{S}_{bl}$ , have more rows than columns, i.e. there are more sources than experiments. Thus, the acquisition can be done in less time.

In the case of source blending the receiver matrix,  $\mathbf{D}$ , is not influenced by blending. And of course, the earth impulse response,  $\mathbf{X}$ , is independent of the acquisition design. Hence, the blended data can be written as;

$$\mathbf{P}_{bl} = \mathbf{D} \mathbf{X} \mathbf{S}_{bl} = \mathbf{D} \mathbf{X} \mathbf{S} \boldsymbol{\Gamma} = \mathbf{P} \boldsymbol{\Gamma}. \quad (2-4)$$

Note that, the blended data matrix,  $\mathbf{P}_{bl}$ , also has less columns, i.e. less experiments, than the unblended data matrix,  $\mathbf{P}$ .

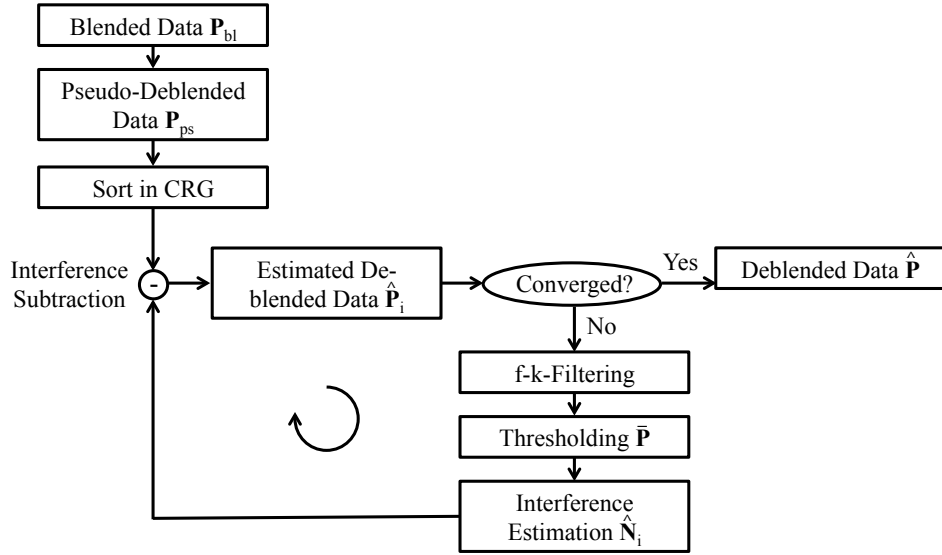


**Figure 2-5:** Flowchart belonging to the deblending method of [Mahdad et al. \(2011\)](#).

## 2-2 Deblending

Before removing the receiver matrix,  $\mathbf{D}$ , and the source matrix,  $\mathbf{S}$ , one must remove the blending matrix,  $\mathbf{\Gamma}$ , from the blended data,  $\mathbf{P}_{bl}$ . This process is called deblending.

The deblending method presented in this thesis builds on the method of [Mahdad et al. \(2011\)](#). Therefore, the method of [Mahdad et al. \(2011\)](#) is described in great detail.

The basic workflow of the method of [Mahdad et al. \(2011\)](#) is summarized in Figure 2-5 and will be explained step by step in the following subsections.

### 2-2-1 Pseudo-Deblending

Unfortunately, the inverse problem of equation 2-4 is underdetermined, which means that there is not a unique solution for the unblended data,  $\mathbf{P}$ . Thus, additional constraints are required to deblend the data, which are (1) sparsity of the signal in the  $x$ - $t$ -domain and (2) coherency of the signal in the  $f$ - $k$ -domain.

The first estimate of the unblended data matrix,  $\mathbf{P}$ , is obtained by pseudo-deblending;

$$\mathbf{P}_{ps} = \mathbf{P}_{bl} \mathbf{\Gamma}^H. \quad (2-5)$$

Pseudo-deblending copies the blended data to the locations of all shots present in the blended shot and shifts them upward in time to compensate for the time delay. For example, Figure 2-6a and 2-6b shows the two pseudo-deblended shot gathers of the blended data in Figure 2-4. Note that the pseudo-deblended data have the same size as  $\mathbf{P}$ .



**Figure 2-6:** Pseudo-deblended data,  $\mathbf{P}_{ps}$ , sorted in common shot gathers (a,b) and in a common receiver gather (c). The pseudo-deblended data of the right shot (a) and the left shot (b,c) were shifted by different time delays. The overlapping sources map in the pseudo-deblended shot gathers as coherent events, while they map as incoherent spikes in the pseudo-deblended receiver gather.

## 2-2-2 Common Receiver Gather

In Figure 2-6a and 2-6b the interfering shots are coherent. By transforming the data to another domain, e.g. to the common receiver domain, the interfering shots become incoherent and are visible as spiky noise (see Figure 2-6c). Therefore, the interfering shots can be attenuated with a noise filter.

## 2-2-3 Iterative Estimation of Blending Noise

In an ideal case the noise generated by the interfering shots present in the pseudo-deblended data, the so called blending noise, is calculated with the unblended data,

$$\mathbf{N} = \mathbf{P}_{bl} \boldsymbol{\Gamma}^H - \mathbf{P} = \mathbf{P}_{ps} - \mathbf{P}. \quad (2-6)$$

Obviously, in practice the unblended data are unknown and must be estimated by adding extra constraints. The loop shown in Figure 2-5 applies the constraints to reduce the blending noise iteratively until the solution is obtained.

In the following all the quantities which are estimated are indicated with a hat. The steps of the iterative blending noise estimation are demonstrated in Figure 2-7.



**Figure 2-7:** (a) Pseudo-deblended receiver gather. The subfigures (b)-(f) illustrate each step of the deblending algorithm. For better visibility examples from the 5<sup>th</sup> iteration are chosen. (b)  $f\text{-}k$ -spectrum before (top) and after (bottom)  $f\text{-}k$ -filtering, (c)  $f\text{-}k$ -filtered common receiver gather, (d) after thresholding, (e) estimated blending noise, (f) estimated data.



**(a)**  $f$ - $k$ -spectrum of an unblended common shot gather. **(b)** The  $f$ - $k$ -mask is determined by the minimum signal velocity in the subsurface. The white area of the filter equals one, the black area equals zero. Thus, the filter removes data which are mapped outside of the white signal cone.

**Figure 2-8**

### f-k-Filtering

One of the constraints is coherency, i.e. by assuming the blending noise in Figure 2-7a is incoherent it can be removed. For this purpose the data are transformed from the space time to the wavenumber frequency domain where the spiky noise spreads over all wavenumber and frequency components (see Figure 2-7b, top).

The unblended data maps in the  $f$ - $k$ -domain in a cone (see Figure 2-8a). The minimum velocity of the subsurface,  $v_{min}$ , determines the slope of the cone. This means that for a given frequency,  $f$ , the maximum wavenumber inside the cone,  $k_{max}$ , is defined as;

$$k_{max} = \frac{f}{v_{min}}. \quad (2-7)$$

In the marine case the minimum velocity is usually the water velocity,  $v_w = 1500 \text{ m s}^{-1}$ .

A 2D  $f$ - $k$ -filter can be designed that removes all elements outside the cone (see Figure 2-8b). The  $f$ - $k$ -filter removes the part of the blending noise, which maps outside of the signal cone (see Figure 2-7b). Thus, after transforming the data back to the space time domain the amplitudes of the spiky noise are attenuated (see Figure 2-7c).

Note that  $f$ - $k$ -filtering can only reduce spatially unaliased blending noise. In Figure 2-8b the highest spatially unaliased frequency is defined by the point where the white cone intersects with the frequency axis, i.e. at 60 Hz.

The high cut frequency of the  $f$ - $k$ -mask is set according to the highest frequency components in the data. The aliased blending noise will pass the  $f$ - $k$ -filter and will be reduced afterwards by thresholding.

### Thresholding

The second constraint for the estimation of the unblended data is sparsity of the signal in the space time domain.

After  $f$ - $k$ -filtering the spiky noise is attenuated (see Figure 2-7c). Consequently, the signal amplitudes are now stronger than the noise amplitudes. This allows to define a threshold in the  $x$ - $t$  domain, which is larger than the attenuated noise amplitudes and smaller than the highest signal amplitudes. Only amplitudes above the threshold are picked (see Figure 2-7d).

### Interference Estimation

The resulting thresholded data,  $\bar{\mathbf{P}}$ , is used to predict the source interference;

$$\hat{\mathbf{N}}_i = \bar{\mathbf{P}} (\mathbf{\Gamma} \mathbf{\Gamma}^H - \mathbf{I}), \quad (2-8)$$

which is illustrated in Figure 2-7e.

### Blending Noise Subtraction

The estimate of the unblended data matrix  $\hat{\mathbf{P}}_i$  is updated by subtracting the noise from the pseudo-deblended data,

$$\hat{\mathbf{P}}_{i+1} = \mathbf{P}_{ps} - \hat{\mathbf{N}}_i, \quad (2-9)$$

which is shown in Figure 2-7f.

This process is repeated iteratively till convergence is reached. In this context convergence can be defined as the point where the difference  $|\hat{\mathbf{P}}_{i+1} - \hat{\mathbf{P}}_i|$  drops below a predefined limit. Alternatively, one can set a maximum number of iterations.

Figure 2-9 shows the estimate of the unblended data for increasing iterations. At each iteration the blending noise is attenuated further, such that the threshold can be lowered. Hence, the predicted blending noise increases and approaches the true blending noise. The blended shot is successively attenuated.

Note that  $f$ - $k$ -filtering lowers the noise level by removing spatially unaliased blending noise. Next, the lowered noise level enables thresholding to reduce spatially aliased the blending noise. Thus, the combination of  $f$ - $k$ -filtering and thresholding is very powerful.



**Figure 2-9:** Common receiver gather of the estimated data after 1, 5, 10, 15, 20 and 25 iterations.

---

# Chapter 3

---

## Incoherency

In this chapter the blending operator is analyzed in greater detail. Then a measure for incoherency will be introduced and the role of incoherency for deblending will be discussed.

### 3-1 Analysis of the Blending Matrix

In order to optimize the blended acquisition design, one must understand the properties of the blending matrix  $\Gamma$  and its influence on the deblending performance.

The blending matrix  $\Gamma$  determines the pseudo-deblended data,

$$\mathbf{P}_{ps} = \mathbf{P}\Gamma\Gamma^H, \quad (3-1)$$

which are a superposition of the unblended data,  $\mathbf{P}$ , and the blending noise,  $\mathbf{N}$ ,

$$\mathbf{P}_{ps} = \mathbf{P} + \mathbf{N}. \quad (3-2)$$

The more incoherent the blending noise,  $\mathbf{N}$ , the better it can be removed by noise filters.

In the following the effect of the blending matrix,  $\Gamma$ , on the matrix product  $\Gamma\Gamma^H$  and on the pseudo-deblended data is analyzed. For simplicity, it is assumed that all shots are equal in strength and fire the same signature into the earth. This means that the blending matrix,  $\Gamma$ , only contains phase shift terms,  $e^{-j\omega\Delta t}$ , with an amplitude equal to 1 or 0. It is also assumed that each shot is fired only once, unlike e.g. the shot repetition case ([Wu, 2014](#)).

Each row of  $\Gamma$  represents a shot  $k$ , and each column of  $\Gamma^H$  represents a shot  $l$  with a complex conjugated phase term (see Figure 3-1). Hence, each element  $g_{kl}$  of the matrix  $\Gamma\Gamma^H$  is the dot product between the  $k^{th}$  shot and the complex conjugate of the  $l^{th}$  shot.

Consequently, an element  $g_{kl}$  of the matrix product  $\Gamma\Gamma^H$  represents the overlap of the shots  $k$  and  $l$  for all experiments. The main diagonal of  $\Gamma\Gamma^H$  refers to the overlap of each shot with itself, which of course is perfect and therefore equal to 1. The off diagonal elements of  $\Gamma\Gamma^H$  are either 0 if the associated shots do not overlap, or contain a phase shift,  $e^{-j\omega\Delta t_{kl}}$ .

$$\begin{array}{c}
 \text{shot } k \\
 \left[ \begin{array}{|c|c|} \hline e^{-j\omega\Delta t_i} & 0 \\ \hline 0 & e^{-j\omega\Delta t_k} \\ \hline e^{-j\omega\Delta t_j} & 0 \\ \hline 0 & e^{-j\omega\Delta t_l} \\ \hline \end{array} \right] \cdot \left[ \begin{array}{|c|c|c|c|} \hline & & & \text{(shots)} \\ \hline e^{+j\omega\Delta t_i} & 0 & e^{+j\omega\Delta t_j} & 0 \\ \hline 0 & e^{+j\omega\Delta t_k} & 0 & e^{+j\omega\Delta t_l} \\ \hline \end{array} \right]_* = \left[ \begin{array}{|c|c|c|c|} \hline 1 & 0 & e^{-j\omega\Delta t_{ij}} & 0 \\ \hline 0 & 1 & 0 & e^{-j\omega\Delta t_{kl}} \\ \hline e^{-j\omega\Delta t_{ji}} & 0 & 1 & 0 \\ \hline 0 & e^{-j\omega\Delta t_{lk}} & 0 & 1 \\ \hline \end{array} \right]
 \end{array}$$

$\Gamma$                            $\Gamma^H$                            $\Gamma\Gamma^H$

**Figure 3-1:** Illustration of the matrix product,  $\Gamma\Gamma^H$ . In this notation  $\Delta t_k$  refers to the phase shift of the shot  $k$ , and  $\Delta t_{kl}$  refers to the phase shift between the shots  $k$  and  $l$ ,  $\Delta t_{kl} = \Delta t_k - \Delta t_l$ .

### Temporal incoherency

In the following the term "sub-diagonal" will be used to refer to an arbitrary diagonal of the matrix  $\Gamma\Gamma^H$ . For example, the  $d^{\text{th}}$  sub-diagonal includes all the matrix elements  $g_{ij}$ , which fulfill the condition;

$$j - i = d. \quad (3-3)$$

In equation 3-1 the main diagonal elements of  $\Gamma\Gamma^H$  copy the data matrix,  $\mathbf{P}$ , while the off-diagonal elements create the blending noise,  $\mathbf{N}$ . In case of a coherent firing time delay the elements along a sub-diagonal  $d$  are in phase. This means that the sub-diagonal elements will shift the columns of the data matrix and apply a coherent phase shift to each of them resulting in the pseudo-deblended receiver gather shown in Figure 3-2a. Instead if the elements  $g_{ij}$  along a sub-diagonal  $d$  are out of phase, they will shift the columns of the data matrix and distort the phase of each column (see Figure 3-2b).

Figure 3-2c and 3-2d display the  $f$ - $k$ -spectra of the pseudo-blended data for constant firing time delays and random firing time delays respectively. In the case of constant firing time delays almost all of the energy maps in the signal cone. In the case of random firing time delays a significant part of the energy maps outside of the signal cone. Therefore, the coherency constraint requires random firing time delays.

In this thesis the random firing time delays are referred to as temporal incoherency.

### Spatial incoherency

Of course, the degree of incoherency of the blending noise,  $\mathbf{N}$ , also depends on whether the shots blended in an experiment are selected randomly, or in a spatially coherent pattern. For example, one expects the blending noise to be more incoherent if in each experiment randomly picked shots are blended, than if in each experiment adjacent shots are blended, because the interfering shots are now spread over the sub-diagonals (see Figure 3-3).

In this thesis selecting random shots for an experiment is referred to as spatial incoherency.



**Figure 3-2:** Comparison of the pseudo-deblended receiver gather for (a) constant firing time delays of 100 ms, and (b) random firing time delays between 0 ms and 100 ms. (c) and (d) show the  $f$ - $k$ -spectra of (a) and (b) respectively.

$$\begin{array}{c}
 \begin{array}{|c|c|} \hline
 e^{-j\omega\Delta t_i} & 0 \\ \hline
 0 & e^{-j\omega\Delta t_k} \\ \hline
 0 & e^{-j\omega\Delta t_l} \\ \hline
 e^{-j\omega\Delta t_j} & 0 \\ \hline
 \end{array} \cdot \begin{array}{|c|c|c|c|} \hline
 & \text{shot } k & & \\ \hline
 & * & & \\ \hline
 e^{+j\omega\Delta t_i} & 0 & 0 & e^{+j\omega\Delta t_j} \\ \hline
 0 & e^{+j\omega\Delta t_k} & e^{+j\omega\Delta t_l} & 0 \\ \hline
 \end{array} = \begin{array}{|c|c|c|c|} \hline
 1 & 0 & 0 & e^{-j\omega\Delta t_{ij}} \\ \hline
 0 & 1 & e^{-j\omega\Delta t_{kl}} & 0 \\ \hline
 0 & e^{-j\omega\Delta t_{lk}} & 1 & 0 \\ \hline
 e^{-j\omega\Delta t_{ji}} & 0 & 0 & 1 \\ \hline
 \end{array} \\
 \Gamma \qquad \qquad \qquad \Gamma^H \qquad \qquad \qquad \Gamma \Gamma^H
 \end{array}$$

**Figure 3-3:** The blending matrix,  $\Gamma$ , is obtained by interchanging the 3<sup>rd</sup> and 4<sup>th</sup> row of the blending matrix in Figure 3-1. In acquisition this is equivalent to moving shot 3 to experiment 2, and shot 4 to experiment 1. A random permutation of the rows of the blending matrix spreads the off-diagonal elements of the matrix product,  $\Gamma \Gamma^H$ . The elements are not assembled on the sub-diagonals anymore.

In practice in 2D blending shots cannot be blended in a spatially incoherent fashion, at least not in a conventional 2D marine acquisition design. In the chapter 4 it will be shown that blending in 3D allows to blend shots spatially incoherent within the crossline direction.

In this chapter spatial incoherency will be illustrated with 2D synthetic data, where the acquisition design is not constraint by practicability.

## 3-2 Effect of Incoherency

An incoherent blending pattern is crucial for good deblending performance (see section 3-1). Thus, a measure of incoherency and deblending quality will be introduced. Then, the possibilities of creating an incoherent blending pattern are presented. Finally, the effect of incoherency on the deblending quality will be shown on a synthetic data set.

### Incoherency Measure

Move this sentence to the introduction (literature). You might also want to mention the work of the Greek guy Apostolos.

In this thesis only the incoherency of the acquisition design is considered. Thus, the blending matrix,  $\Gamma$ , or more precisely the product  $\Gamma\Gamma^H$  determines the incoherency.

A measure of incoherency will be introduced in order to analyze the importance of an incoherent blending pattern quantitatively.

In section 3-1 it was shown that for an incoherent blending pattern the elements,  $e^{-j\omega\Delta t_{kl}}$ , along a sub-diagonal of the matrix product  $\Gamma\Gamma^H$  should be out of phase. Therefore, the phase variability of the sub-diagonal elements will be used to quantify incoherency.

Note that the sub-diagonal elements,  $e^{-j\omega\Delta t_{kl}}$ , map in the complex plane on a circle with radius 1 (see Figure 3-4).

The sum of the elements along the  $d^{th}$  sub-diagonal can be constructive or destructive, depending on the phase variability. Thus, the absolute value of the sum,  $S(d, \omega)$ , measures the incoherency of an individual sub-diagonal. The sum,  $S(d, \omega)$ , is a function of the sub-diagonal  $d$  and the frequency component,  $\omega$ ;

$$S(d, \omega) = \left| \sum_{j-i=d} \Gamma\Gamma_{ij}^H(\omega) \right|. \quad (3-4)$$

For example, if all elements are in phase the absolute value of their sum,  $S(d, \omega)$ , is maximized. The more the elements are out of phase, i.e. the more incoherent they are, the smaller is  $S(d, \omega)$ . Thus, in case of an incoherent blending pattern  $S(d, \omega)$  is small for all sub-diagonals  $d$ , except for the main diagonal,  $d = 0$ .

All frequency components,  $\omega$ , of  $S(d, \omega)$  are summed. The resulting function,  $S(d)$ , only depends on the sub-diagonal number. Next, each element of  $S(d)$  is squared to relate it to energy.

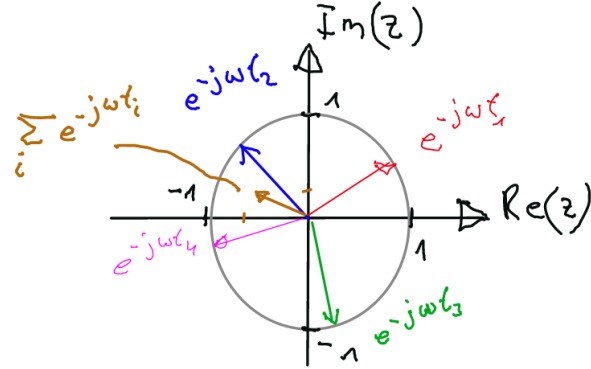


**Figure 3-4:** Illustration of the sub-diagonal elements in the complex number plane. The elements have unit length and variable phase. The absolute value of their sum depends on the phase coherency of the elements.

The incoherency,  $\mu$ , is quantified by the ratio of the main diagonal and the sum of all sub-diagonals;

$$\mu = \frac{(\sum_{\omega} S(d=0, \omega))^2}{\sum_{d=1-N_s}^{N_s-1} (\sum_{\omega} S(d, \omega))^2} \quad (3-5)$$

Consider the two blending matrices,  $\mathbf{\Gamma}_{coh}$  and  $\mathbf{\Gamma}_{ran}$ , which produced the pseudo-deblended receiver gathers in Figure 3-2a and 3-2b. The blending matrix,  $\mathbf{\Gamma}_{coh}$ , uses coherent firing time delays, while the blending matrix,  $\mathbf{\Gamma}_{ran}$ , uses random firing time delays. Figure 3-5 shows  $S(d, \omega)$  for both blending matrices for the frequency slice  $f = 25$  Hz.

The closer Figure ?? comes to a spike the more incoherent is the blending pattern. Thus, considering Figure ?? the incoherency,  $\mu$ , is measured as the ratio between the amplitude of the spike and the sum of all amplitudes.

In terms of the sub-diagonals of  $\mathbf{\Gamma}\mathbf{\Gamma}^H$  this is the ratio between the squared absolute value of the summed main diagonal and the sum of all squared absolute summed sub-diagonals;

$$\mu(\omega) = \frac{\left| \sum_{j-i=0} \mathbf{\Gamma}\mathbf{\Gamma}_{ij}^H(\omega) \right|^2}{\sum_{k=1-N_s}^{N_s-1} \left( \left| \sum_{j-i=k} \mathbf{\Gamma}\mathbf{\Gamma}_{ij}^H(\omega) \right|^2 \right)}. \quad (3-6)$$

Note that  $N_s$  is the number of sources, i.e. the matrix  $\mathbf{\Gamma}\mathbf{\Gamma}^H$  has  $N_s$  rows and columns.

Up to now, the incoherency is computed for each frequency separately. In order to account for all frequencies at once the nominator and denominator in equation 3-6 are summed over all frequency components;

$$\mu = \frac{\sum_{\omega} \left( \left| \sum_{j-i=0} \mathbf{\Gamma}\mathbf{\Gamma}_{ij}^H(\omega) \right|^2 \right)}{\sum_{\omega} \left( \sum_{k=1-N_s}^{N_s-1} \left( \left| \sum_{j-i=k} \mathbf{\Gamma}\mathbf{\Gamma}_{ij}^H(\omega) \right|^2 \right) \right)}. \quad (3-7)$$

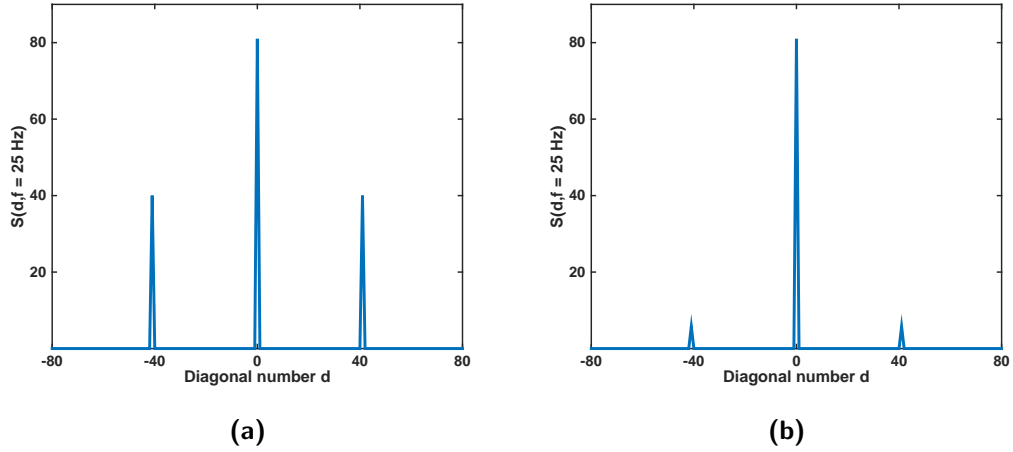


**Figure 3-5:** Illustration of the absolute sub-diagonal sums,  $S(d, \omega)$ , for the frequency slice  $f = 25 \text{ Hz}$ . (a) refers to the blending matrix  $\Gamma_{coh}$  with coherent firing time delays.  $S(d, \omega)$  is less spike-like and yields an incoherency value of  $\mu_a = 67\%$ . (b) refers to the blending matrix  $\Gamma_{ran}$  with random firing time delays.  $S(d, \omega)$  is close to a spike and yields an incoherency value of  $\mu_b = 98\%$ .

For example, for a perfectly incoherent blending pattern only the sum along the main diagonal ( $k = 0$ ) is non zero. Thus, the nominator and the denominator in equation 3-5 are identical, the incoherency equals 1.

In contrast, for a perfectly coherent blending pattern all sub-diagonal elements are in phase. Consequently, the sum along the main diagonal is of the same magnitude as the sum along the sub-diagonals. The nominator in equation 3-5 becomes significantly smaller than the denominator, and the incoherency is nearly 0.

### 3-3 Results

#### 3-4 Effect of Maximum Firing Time Delay

#### 3-5 Results

---

## Chapter 4

---

# Crossline Deblending (3D)

This thesis suggests to blend crossline sources, i.e. in combination with the movement of the seismic vessel one effectively blends sources in 3D.

In this paragraph I use the word "source". For consistency I thought about using the word "shot". However, it seems to sound strange in this sentence.

The deblending method of [Mahdad et al. \(2011\)](#) described in section [2-2](#) is designed for 2D blended data. In this thesis I will explain how each step of the Mahdad method can be applied to 3D data as well, and I will demonstrate its performance.

First, the data sorting will be modified such that the blended 3D data can be described using the same forward model as in section [2-1](#). The presented data sorting will allow to maintain all other steps of the deblending algorithm of [Mahdad et al. \(2011\)](#) unchanged. Second, the  $f$ - $k$ -filter will be extended to an  $f$ - $k_x$ - $k_y$ -filter to remove noise in crossline and inline direction.

### 4-1 Data Sorting

#### Data Matrix

In 3D acquisition the sources and receivers are distributed on a 2D surface. Thus, their locations are defined by their crossline and inline positions,  $(x, y)$ . Each data point which is measured by a source receiver pair at a specific time is therefore described by 5 coordinates, time  $t$ , receiver crossline and inline position  $(x_r, y_r)$ , and source crossline and inline position  $(x_s, y_s)$ .

The 5D data "cube" will be again reorganized in a 2D data matrix according to [van Dedem \(2002\)](#) (see Figure [4-1](#)). For this data sorting a 1D Fourier transform with respect to time is performed and a 4D frequency "slice" is selected.

The 4D "slice" is sorted in a 2D data matrix,  $\mathbf{P}$ , with as many rows as receivers and as many columns as shots. The total number of shots is obtained by multiplying the number of shots

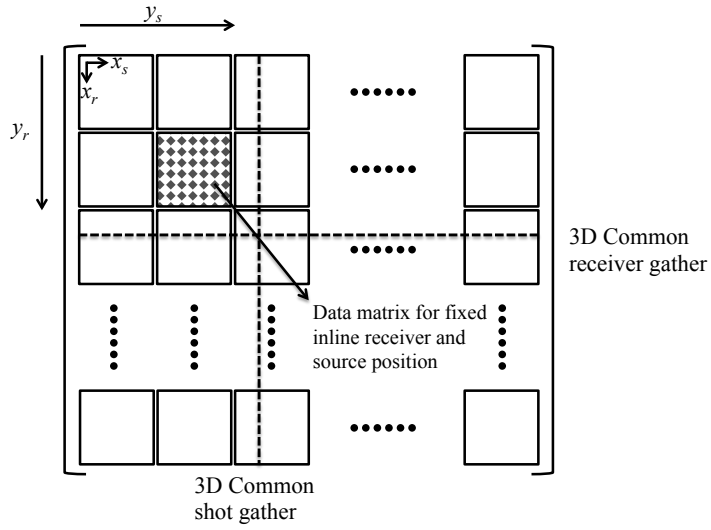


**Figure 4-1:** Illustration of the data matrix  $\mathbf{P}$  for 3D data (van Dedem, 2002).  $y_r$  and  $y_s$  represent the inline receiver and source positions.  $x_r$  and  $x_s$  represent the crossline receiver and source positions. Each row refers to a 3D common receiver gather and each column to a 3D common shot gather. A sub-matrix with fixed receiver and source inline positions ( $y_r, y_s$ ) is equivalent to a data matrix for 2D acquisition.

fired in each crossline and the number of shots fired in each inline. The total number of receivers is obtained likewise. Assume there are  $Ns_x$  shots per crossline. The shots of the first crossline are assigned to the first  $Ns_x$  columns of the data matrix, the shots of the second crossline are assigned to the next  $Ns_x$  columns of the data matrix, etc. The cross- and inline receivers are sorted in the rows of the data matrix in analogy.

For example, one row in the data matrix,  $\mathbf{P}$ , in Figure 4-1 represents a common receiver gather. The data of this common receiver gather are shown in Figure 4-2a, where the coordinates,  $x$  and  $y$ , indicate the crossline and inline shot position respectively. For the described data sorting individual crossline slices are extracted from this data cube and assembled next to each other in a data matrix as shown in Figure 4-2b. Each hyperbolic event refers to the response of the shots of one crossline.

### Blending matrix

The blending matrix for 3D is build in a similar fashion as the data matrix in 3D. As described in section 3-1 each row of the blending matrix,  $\mathbf{\Gamma}$ , captures one shot. For extension to 3D the shots of the first crossline are placed in the top  $Ns_x$  rows of the blending matrix, followed by the shots of the second crossline etc. (see Figure 4-3). The elements in the  $j^{th}$  column of the blending matrix,  $\mathbf{\Gamma}$ , select the shots which are blended in the  $j^{th}$  experiment. For example, the first column of the blending matrix in Figure 4-3b describes that in the first experiment shots 1 and 3 are blended with a time delay of  $\Delta t_1$ .

Keep this sentence for later: This framework allows to blend any source combination independent of the cross- and inline positions of the involved sources.

With the new data and blending matrix sorting one can apply deblending to 3D data.

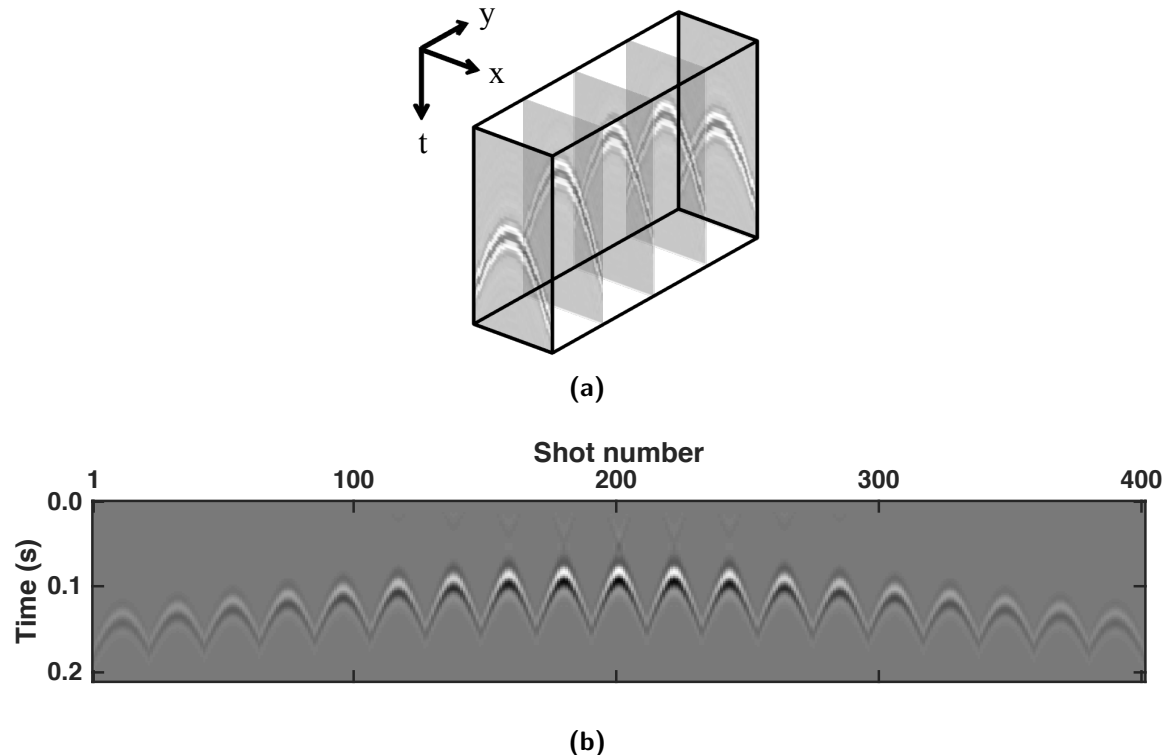


**Figure 4-2:** (a) Common receiver gather of a 3D data set with crossline ( $x$ ) and inline ( $y$ ) sources.  
 (b) Resorting data set. Individual crossline sections are plotted next to each other in 2D. For visibility both subfigures only show a reduced part of the data.

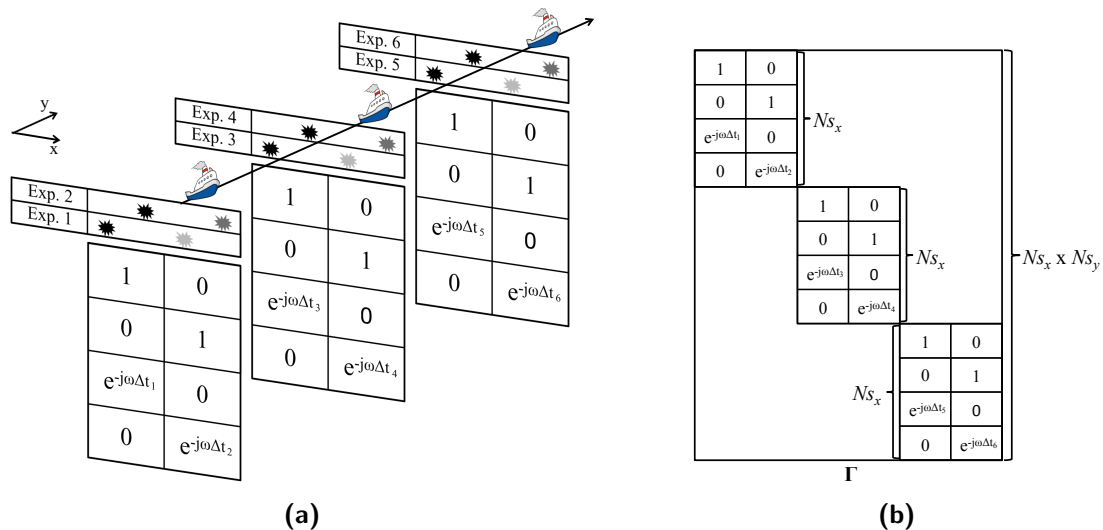


**Figure 4-3:** Illustration of the blending matrix,  $\Gamma$ , for 3D acquisition. (a) At each of the  $Ns_y$  inline position the crossline sources ( $x$  direction) are blended. Each of these 2D blending processes is described by a 2D blending matrix, which has as many rows as there are crossline sources,  $Ns_x$ . (b) The 2D blending matrices are assembled in a single 3D blending matrix,  $\Gamma$ , which has  $Ns_x$  by  $Ns_y$  rows.

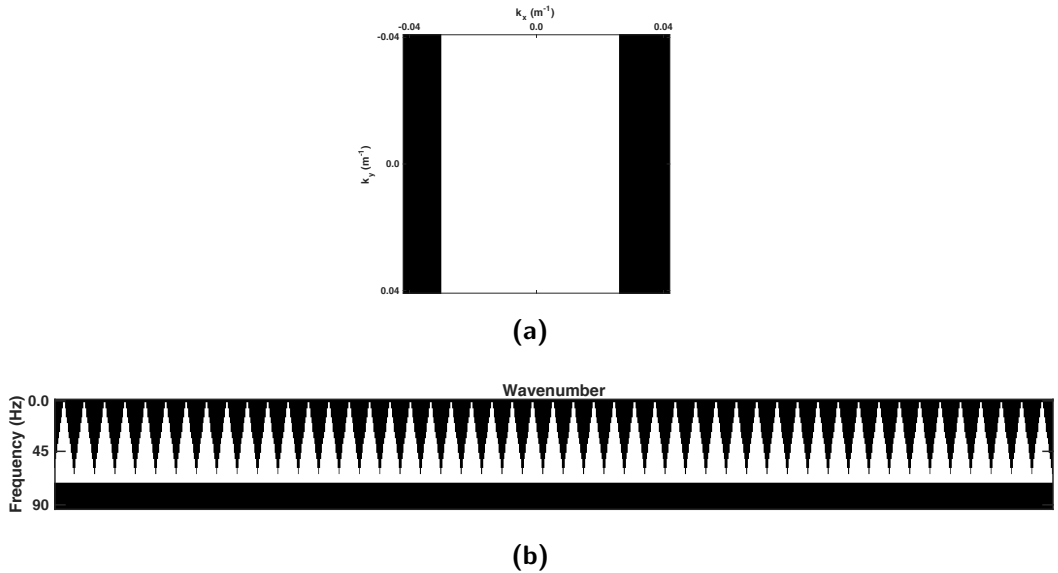


**Figure 4-4:** One can design a 2D  $f\text{-}k_x$ -filter for 3D data. (a) shows a 40 Hz frequency slice of the  $f\text{-}k_x\text{-}k_y$  spectrum, where the white area equals 1 and the black area is 0. Note that the filter is not affecting the inline wavenumbers  $k_y$ . (b) illustrates the 2D  $f\text{-}k_x$ -filter sorted according to section 4-1. Each cone represents a 2D  $f\text{-}k$ -filter for a single inline wavenumber.

## 4-2 3D f-k-k Filter

In section 2-2-3 the 2D  $f\text{-}k$  filter was introduced. By sorting the 2D  $f\text{-}k$ -filter according to section 4-1 it can be applied to 3D data.

For this purpose one considers a 3D common receiver gather,  $\mathbf{p}(t, x_s, y_s)$ , and brings it to the  $f\text{-}k_x\text{-}k_y$  domain by applying a 3-dimensional Fourier transform. Next, a constant frequency slice is selected. This leaves a 2D matrix, which captures the cross- and inline wavenumbers  $(k_x, k_y)$ . The maximum crossline wavenumber,  $k_x$ , is defined according to section 2-2-3. The resulting  $f\text{-}k$ -mask is shown in Figure 4-4. Note that it only filters the crossline wavenumbers  $k_x$ , i.e. it is a  $f\text{-}k_x$  filter.

The  $f\text{-}k_x\text{-}k_y$  spectra of synthetic data shown in Figure 4-5a and 4-5d illustrate that the 2D  $f\text{-}k_x$ -filter will also pass some energy which is not signal. In the following both spatial directions,  $x$  and  $y$ , are considered to extend the filter to a 3D  $f\text{-}k_x\text{-}k_y$ -filter.

The starting point is a frequency slice of the  $f\text{-}k_x\text{-}k_y$  spectrum as shown in Figure 4-5a. Again the minimum velocity,  $v_{min}$ , and the frequency,  $f$ , determine the maximum wavenumber,  $k_{max}$ , according to equation 2-7. The total wavenumber,  $k_T$ , must be smaller than the maximum wavenumber,  $k_{max}$ ,

$$k_T = \sqrt{k_x^2 + k_y^2} < k_{max}. \quad (4-1)$$

Hence the signal "cone" is defined by a circle (see Figure 4-5c). This is repeated for each frequency component, such that the overall  $f\text{-}k_x\text{-}k_y$ -mask is a 3D cone (see Figure 4-5). Finally, this mask is computed for each receiver gather.

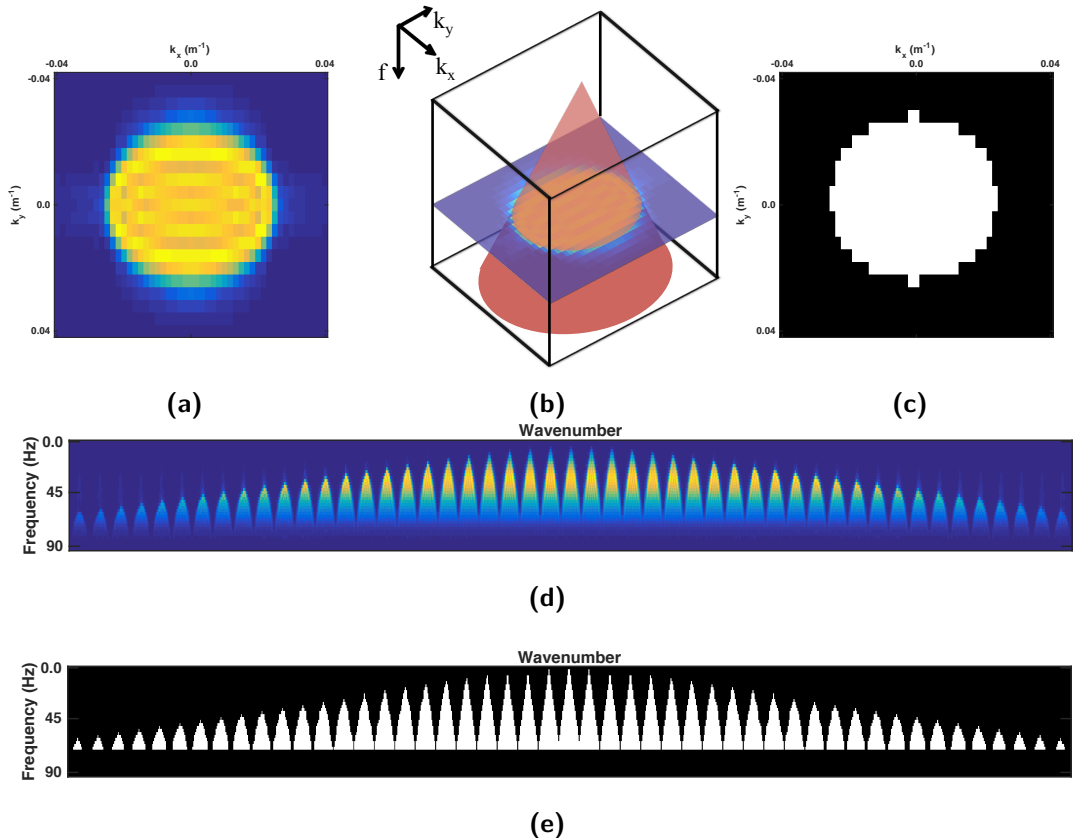


**Figure 4-5:** Illustration of the 3D  $f\text{-}k_x\text{-}k_y$ -filter. (a) is a 40 Hz frequency slice of the  $f\text{-}k_x\text{-}k_y$  spectrum of the data in Figure 4-2b.  $k_x$  and  $k_y$  refer to the crossline and inline wavenumber respectively. (b) shows the same data slice sorted in a 3D cube. The red cone represents the 3D  $f\text{-}k_x\text{-}k_y$  filter mask. (c) is a 40 Hz frequency slice of the mask, where the white area equals 1 and the black area is 0. (d) and (e) display the  $f\text{-}k_x\text{-}k_y$  data spectrum and mask sorted according to section 4-1, i.e. each sub-cone refers to one inline wavenumber. Note that due to the sorting the wavenumber axis is a mix of crossline and inline wavenumbers. For this reason the wavenumber axis has no labels.

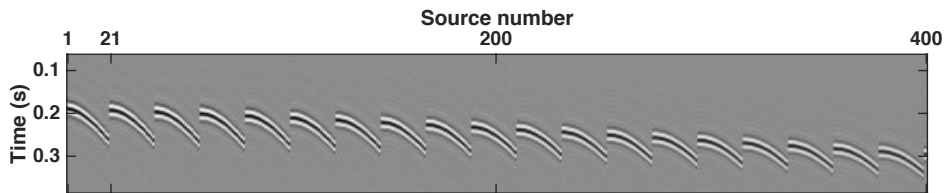
### 4-3 Results

The 3D  $f\text{-}k_x\text{-}k_y$  filter removes incoherent energy in the crossline and inline direction. The suggested 3D blended acquisition design blends sources within the same crossline. Hence, the question arouses whether an extension of the 2D  $f\text{-}k_x$  filter to the inline direction provides significant deblending enhancements.

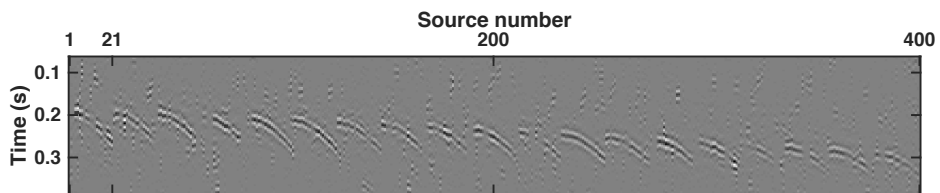
For this purpose the synthetic data of Figure 4-6a are blended: Within each crossline there are 21 sources, which are blended in 3 experiments. For each experiment 7 randomly selected sources are blended with random time delays, i.e. the blending pattern with mixed incoherency is applied. The maximum allowed firing time delay is set to 400 ms.

The blended data are deblended with the 3D deblending algorithm. In one case a 2D  $f\text{-}k_x$  filter is applied (see Figure 4-6b). In the other case a 3D  $f\text{-}k_x\text{-}k_y$  filter is applied (see Figure 4-6c). It is clearly visible that the deblending quality increases significantly with the 3D  $f\text{-}k_x\text{-}k_y$  filter.

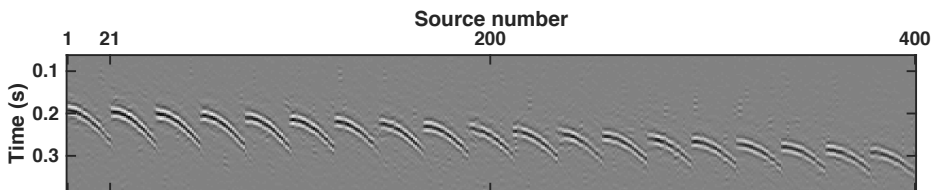
In order to quantify the quality gap between the results with 2D and 3D filters, the data of Figure 4-6a are blended with maximum firing time delays varying between 40 ms and 400 ms. The blended data are deblended in one case with a 2D  $f\text{-}k$  filter, and in the other case with a 3D  $f\text{-}k_x\text{-}k_y$  filter. The resulting quality factors are shown in Figure 4-7.



**(a)** Unblended synthetic data. These data show a common receiver gather, which is generated by 21 crossline shots and 51 inline shots. The shown section is a zoom on the strongest events.



**(b)** Deblending result with a 2D  $f\text{-}k_x$  filter



**(c)** Deblending result with a 3D  $f\text{-}k_x\text{-}k_y$  filter

**Figure 4-6:** The crossline sources of the synthetic data in Figure 5-1a are blended. Then, the 3D deblending algorithm is applied. In case (a) the algorithm uses a 2D  $f\text{-}k_x$  filter. In case (b) it uses a 3D  $f\text{-}k_x\text{-}k_y$  filter.

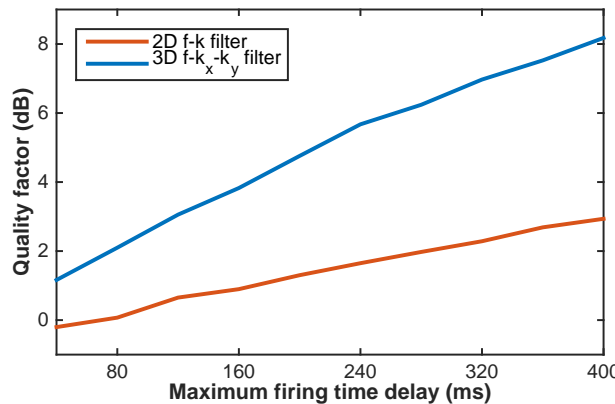


**Figure 4-7:** Comparison of the deblending quality with a 2D  $f\text{-}k_x$  filter and a 3D  $f\text{-}k_x\text{-}k_y$  filter. The data in Figure 4-6a are blended with varying maximum firing time delay. Then the blended data are deblended using a 2D  $f\text{-}k_x$  filter and a 3D  $f\text{-}k_x\text{-}k_y$  filter.



---

# Chapter 5

---

## Results on Synthetic Data

This chapter presents the major results of this thesis. First, an optimal blending pattern for simultaneous crossline sources will be derived. Then, the advantages of a 3D  $f\text{-}k_x\text{-}k_y$ -filter towards a 2D  $f\text{-}k$ -filter will be shown. Finally, the feasibility of the suggested acquisition design will be proven on a synthetic 3D data set.

### 5-1 Blending pattern

An incoherent blending pattern is crucial for good deblending performance (see section 3-1). Thus, a measure of incoherency and deblending quality will be introduced. Then, the possibilities of creating an incoherent blending pattern are presented. Finally, the effect of incoherency and of the maximum firing time delay on the deblending performance will be demonstrated.

#### Deblending Performance Measure

The following data examples are synthetic data, i.e. the unblended data is known. Therefore, the deblending performance can be measured with the quality factor,  $Q$ , which is defined by [Ibrahim and Sacchi \(2015\)](#) as;

$$Q = 10 \cdot \log_{10} \left( \frac{\|\text{Unblended data}\|_2^2}{\|\text{Unblended data} - \text{Deblended data}\|_2^2} \right) . \quad (5-1)$$

#### Incoherent Blending Patterns

This thesis considers the following blended acquisition set up: The sources are assembled in crossline direction and move towards inline direction due to the vessel movement (see Figure 4-3a). As a consequence each experiment can blend sources which belong to the same

crossline. The inline source sampling rate must be sufficiently small to avoid spatial aliasing. Thus, the sources within one crossline must be blended and recorded before the vessel reaches the next inline position.

Based on this set up there are three possibilities to blend the sources incoherently. First, the sources can be blended with random time delays (temporal incoherency). Second, one can randomly pick sources for each experiment (spatial incoherency). Third, temporal and spatial incoherency can be combined (mixed incoherency), i.e. randomly picked sources are blended with random time delays.

In the following these blending patterns will be applied to a synthetic data set (see Figure 5-1a, 5-2a, 5-2e). Next, the data is deblended with the 3D deblending algorithm of chapter 4.

The deblending results are shown in Figure 5-1 and 5-2. The results suggest that only spatial incoherency is not sufficient to deblend the data (see Figure 5-1b, 5-2b, 5-2f). By introducing random firing time delays the deblended data improves significantly as shown in Figure 5-1c, 5-2c, 5-2g). A combination of both spatial and temporal incoherency enhances the deblended data further (see Figure 5-1d, 5-2d, 5-2h).

Make a sketch of the set up of the synthetic data.

## Effect of Incoherency

The above comparison of incoherencies distinguishes different incoherency types. However, each of these types has a different degree of incoherency,  $\mu$ . Therefore, the dependence of the deblending quality,  $Q$ , on the incoherency,  $\mu$ , will be analyzed.

For this purpose blending matrices with incoherencies between 5 % and 100 % are generated. Next, synthetic data is blended and deblended with these blending matrices. The quality factor,  $Q$ , is computed for each deblended data set. Figure 5-3 illustrates the resulting quality factor as a function of the incoherency.

This result demonstrates that a good deblending result requires an incoherent deblending pattern, but the deblending quality is not very sensitive to the incoherency. In plain English, either the degree of incoherency is sufficiently high or not. Therefore, the incoherency degree is crucial ingredient, but it is not a suitable parameter to fine tune the desired quality factor.

## Effect of Maximum Firing Time Delay

Another control factor of the deblending performance is the maximum firing time delay. In an extreme case of infinitely long maximum firing time delay the acquisition is not blended any more, and the deblending result is perfect. Hence, increasing maximum firing time delays are expected to enhance the deblending quality, but they require more acquisition time.

The three suggested blending patterns namely temporal, spatial and mixed incoherency are applied to synthetic data with varying maximum firing time delays.

Figure 5-4 shows the quality factors for the three blending patterns as a function of maximum firing time delay. The spatially incoherent blending pattern yields a constant deblending quality independent of the maximum firing time delay. This is expected because it blends

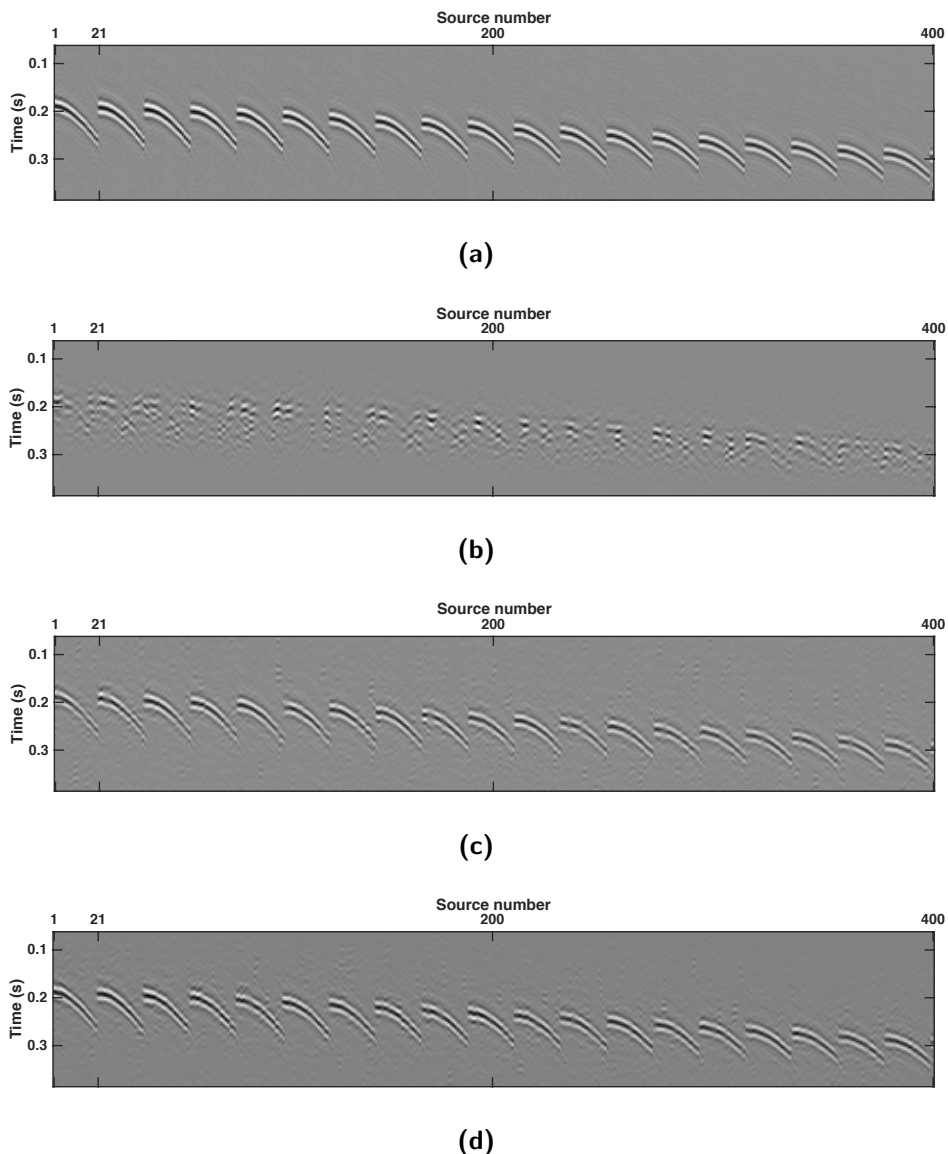


**Figure 5-1:** These 3D common receiver gathers are sorted according to section 4-1. The unblended synthetic data (a) is used to simulate a blended acquisition with 3 experiments per crossline and 7 shots per experiment. The maximum firing time delay is 400 ms. The sources are blended in three different patterns: (b) Randomly selected sources are blended without time delay, (c) neighboring sources are blended with random time delays, (d) randomly picked sources are blended with random time delays. Next, the blended data sets are deblended. The corresponding deblending results are illustrated in (b) to (d).

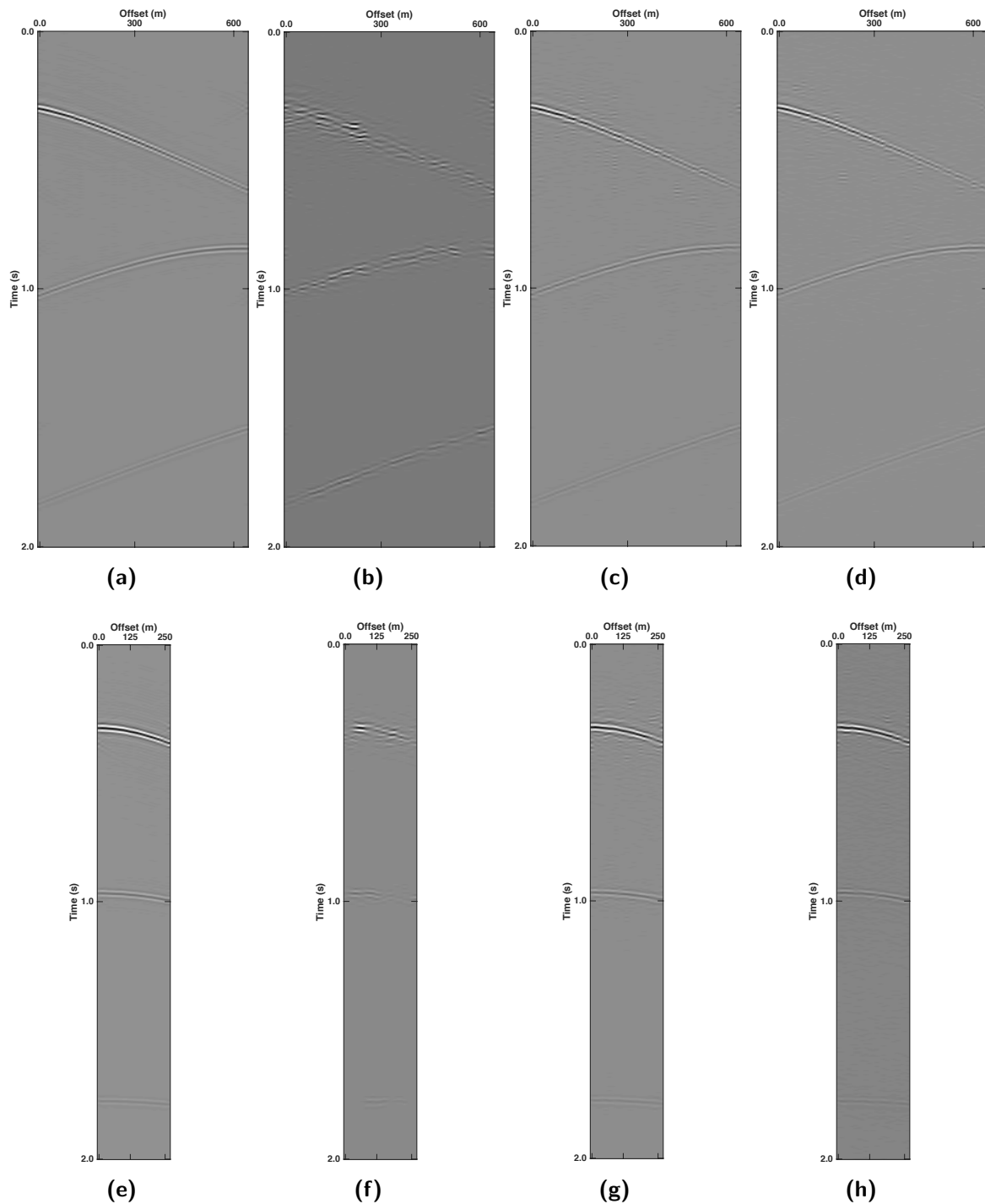


**Figure 5-2:** (a)-(d) show inline slices of the data shown in Figure 5-1. (e)-(h) display the corresponding crossline slices.

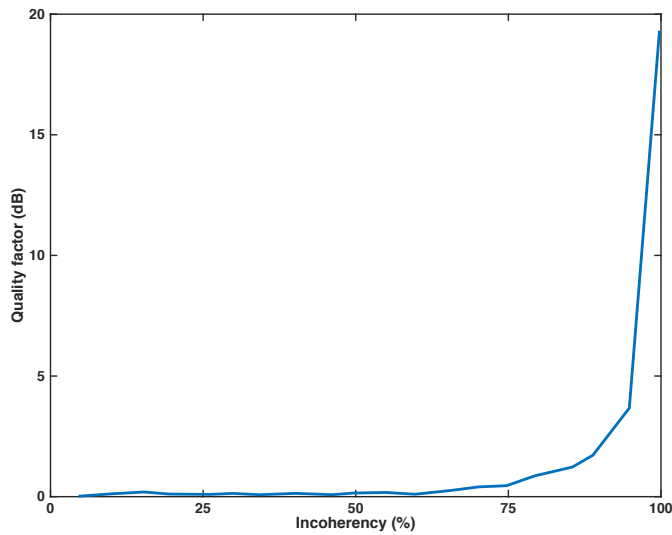


**Figure 5-3:** Quality factor,  $Q$ , as a function of the incoherency,  $\mu$ . The quality factor is a measure for the deblending performance. The deblending results for quality factors above 5 look acceptable.

the sources without time delay. The deblending quality provided by the other two blending patterns continuously enhances with increasing maximum firing time delay. The difference between the deblending quality given by temporal and mixed blending patterns seems to be independent of the maximum firing time delay.

For the conclusion/discussion of these results:

Say that a high degree of incoherency is required for successful deblending, but it is not useful as a control factor of the deblending performance. Instead the maximum firing time delay allows to fine tune the quality factor and might be suitable to fine tune a trade off between deblending quality and acquisition time.

One can also say that the spatial incoherency performs poorly because its degree of incoherency is simply too low.

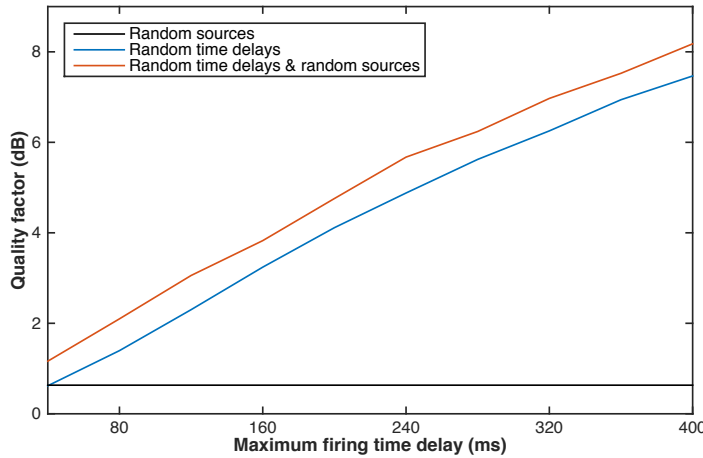


**Figure 5-4:** The 3 suggested blending patterns are simulated with maximum firing time delays between 40 ms and 400 ms. The quality factors are computed with respect to the unblended data and illustrated as a function of the maximum firing time.

## 5-2 Feasibility

The results demonstrate how the 3D deblending result can be optimized. In practice, the sources within a crossline must be fired and recorded before the vessel reaches the next inline position.

It is assumed that the vessel moves with a speed of  $1.2 \text{ m s}^{-1}$ , the recording time per experiment is 3 s and the desired inline spacing is 12.5 m. Thus, the maximum firing time delay can be up to 400 ms.

In the synthetic data in Figure 5-1 the cross- and inline spacing equals 12.5 m. The acquisition set up of the synthetic data is shown in 5-5.

The deblending result in Figure 5-1d fulfills all the conditions of the feasibility test. For a maximum firing time delay of 400 ms the deblending quality is  $Q = 8.6 \text{ dB}$ , which is very good. Therefore, the suggested blended acquisition is feasible for synthetic data.

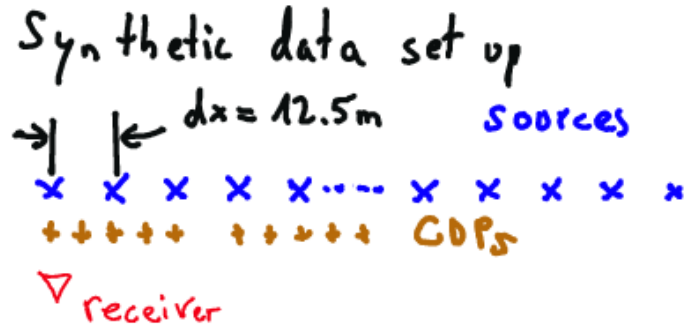


**Figure 5-5:** Illustration of the acquisition design of the synthetic data in Figure 5-1. There are 21 sources in the crossline with a spacing of 12.5 m. At each inline position the crossline sources are blended in 3 experiments with 7 sources per experiment.

---

# Chapter 6

---

## Incoherency

When multiple sources are applied in one experiment the wavefields of the individual sources overlap. [Mahdad et al. \(2011\)](#) presented a method to separate the overlapping wavefields: A key step is pseudo-deblending, which yields the the desired unblended data superimposed by so called blending noise. This noise is generated by the overlap of the individual sources and can be removed with noise filters. However, if the individual wavefields overlap coherently, the blending noise will also be coherent and cannot be removed. In other words it is crucial to fire the sources incoherently.

In this chapter the incoherency of the source overlap is analyzed by considering three questions: Which factors control the incoherency? How can the incoherency be measured? How can the incoherency be maximized for an optimal deblending result?

### 6-1 Incoherency Control Factors

The deblended data can be represented by

$$\mathbf{P}_{\text{debl}} = \mathbf{X} \mathbf{S} \mathbf{\Gamma} \mathbf{\Gamma}^H. \quad (6-1)$$

Each of the matrices in the above equation influences the degree of incoherency of the source overlap. First, the contribution of the Earth  $\mathbf{X}$  is neglected because it cannot be controlled in a seismic experiment. Second, the source signature  $\mathbf{S}$ , in particular its time duration, determines the required minimum time delay between sources to avoid an overlap. Consequently, when designing an acquisition with simultaneous sources one must take into account the source signature. Thirdly, the incoherency is strongly dependent on the blending matrix  $\mathbf{\Gamma}$  because it captures the firing pattern, i.e. it knows which sources are superimposed and the time delays between the sources in a given experiment. Therefore, the main focus of the incoherency analysis will be on the blending matrix  $\mathbf{\Gamma}$ .

## 6-2 Quantification of Incoherency

A mathematical tool to express incoherency is the autocorrelation function  $R(\tau)$ ,

$$R(\tau) = \int_{\mathbb{R}} f^*(x)f(x + \tau) dx. \quad (6-2)$$

For example, in a 1D case the autocorrelation of a fully incoherent function is a spike at zero lag. If a coherent or repetitive pattern is present in a function the autocorrelation will also have non zero amplitudes at other lags.

For comparative purposes the incoherency of a function  $f(x)$  should be quantified. It is suggested to measure incoherency  $\mu$  as the ratio of the squared zero lag autocorrelation and the sum of the squared autocorrelation amplitudes,

$$\mu = \frac{R(\tau = 0)^2}{\sum_{\tau} R(\tau)^2}. \quad (6-3)$$

This expression quantifies incoherency as a number between 0 and 1. A fully incoherent function  $f(x)$  yields an autocorrelation which is a perfect spike. Thus, the ratio in equation 6-3 equals 1. For a perfectly coherent function  $f(x)$  the ratio in equation 6-3 is nearly zero.

The incoherency strongly depends on the blending matrix  $\Gamma$  which is a 3D array. Before applying an autocorrelation the blending matrix  $\Gamma$  is transformed to time domain. The time domain blending matrix is denoted as  $\gamma$ . It has the dimensions

$$\dim(\gamma) = \text{Sources} \times \text{Experiments} \times \text{Time}. \quad (6-4)$$

If a source  $s_i$  is fired in an experiment  $e_i$  at a time  $t_i$  the element  $(s_i, e_i, t_i)$  of  $\gamma$  is 1, else it is 0. If the source is not a perfect spike its amplitude can smear out across several time samples in the matrix  $\gamma$ .

The incoherency of the blending matrix  $\gamma$  can be quantified by replacing the 1D autocorrelation in equation 6-2 and 6-3 with a 3D autocorrelation, which can be written as,

$$R(\tau_1, \tau_2, \tau_3) = \iiint_{\mathbb{R}^3} f^*(x, y, z)f(x + \tau_1, y + \tau_2, z + \tau_3) dx dy dz. \quad (6-5)$$

The calculation of the 3D autocorrelation function requires significant computational power such that symmetry properties of the autocorrelation should be exploited to reduce the cost. Symmetry with respect to the origin, but using convn in Matlab I cannot access it

The elements of the resulting 3D autocorrelation array are a measure for the correlation between wavefields at a specific source, experiment and time lag. For example, if in each experiment adjacent sources are fired with a constant time delay  $\Delta t$ , the 3D autocorrelation will yield a high amplitude at the source lag 1, experiment lag 0 and time lag  $\Delta t$ .

Combining equations 6-3 and 6-5 the incoherency of the time domain blending matrix  $\gamma$  can be expressed as,

$$\mu = \frac{R(\tau_1 = 0, \tau_2 = 0, \tau_3 = 0)^2}{\sum_{(\tau_1, \tau_2, \tau_3)} R(\tau_1, \tau_2, \tau_3)^2}. \quad (6-6)$$

### 6-3 Optimization of Incoherency

Relate the incoherency estimate to the quality factor of the deblending. Point out that the quality factor is very sensitive to the time incoherency while the incoherency with respect to experiments or sources has less impact on the deblending performance.

### 6-4 Fingerprint of the Incoherency in the Blending Matrix $\Gamma$

To achieve a better understanding of the blending process the relation between the incoherency quantification and the blending matrix  $\Gamma$  is assessed.

In frequency domain the blending matrix has the dimension,

$$\dim(\boldsymbol{\Gamma}) = \text{Sources} \times \text{Experiments} \times \text{Frequency}, \quad (6-7)$$

where each element is a complex number  $a e^{-j\omega t}$ .

Mahdad et al. (2011)

---

## Bibliography

- Berkhout, A. (1982). *Seismic Migration: Imaging of Acoustic Energy by Wave Field Extrapolation, Part A: Theoretical Aspects*. Elsevier.
- Ibrahim, A. and Sacchi, M. D. (2015). Fast simultaneous seismic source separation using stolt migration and demigration operators. *researchgate.net*.
- Mahdad, A., Doulgeris, P., and Blacquiere, G. (2011). Separation of blended data by iterative estimation and subtraction of blending interference noise. *Geophysics*, 76(3):Q9–Q17.
- van Dedem, E. J. (2002). *3D surface-related multiple prediction*. PhD thesis, TU Delft.
- van Groenestijn, G. J. A. (2010). *Estimation of Primaries and Multiples by Sparse Inversion*. PhD thesis, TU Delft.
- Wu, S. (2014). Seismic deblending by shot repetition. Master's thesis, TU Delft.



---

# Appendix A

---

## The back of the thesis

### A-1 An appendix section

#### A-1-1 An appendix subsection with C++ Listing

```
//  
// C++ Listing Test  
//  
#include <stdio.h>  
for( int i=0;i<10;i++)  
{  
    cout << "Ok\n";  
}
```

1  
6

#### A-1-2 A Matlab Listing

```
%  
% Comment  
%  
n=10;  
for i=1:n  
    disp('Ok');  
end
```

5



---

## Appendix B

---

# Yet another appendix

### B-1 Another test section

Ok, all is well.

---

# **Index**

LaTeX, 1